Journal of Nuclear Materials 485 (2017) 231–242

Contents lists available at ScienceDirect

Journal of Nuclear Materials

journal homepage: www.elsevier.com/locate/jnucmat

A dislocation-based crystal viscoplasticity model with application to micro-engineered plasma-facing materials

David Rivera, Yue Huang, Giacomo Po, Nasr M. Ghoniem*

Department of Mechanical & Aerospace Engineering, University of California at Los Angeles (UCLA), 420 Westwood Plaza, Los Angeles, CA 90095-1597, USA

ARTICLE INFO

Article history:
Received 25 September 2016
Received in revised form
20 November 2016
Accepted 28 December 2016
Available online 30 December 2016

Keywords:
Tungsten
Thermomechanics
Plasma transients
Surface architecture
Residual stress

ABSTRACT

Materials developed with special surface architecture are shown here to be more resilient to the transient thermomechanical environments imposed by intermittent exposures to high heat flux thermal loading typical of long-pulse plasma transients. In an accompanying article, we present experimental results that show the relaxation of residual thermal stresses in micro-engineered W surfaces. A dislocation-based model is extended here within the framework of large deformation crystal plasticity. The model is applied to the deformation of single crystals, polycrystals, and micro-engineered surfaces composed of a uniform density of micro-pillars. The model is utilized to design tapered surface micro-pillar architecture, composed of a Re core and W coatings. Residual stresses generated by cyclic thermomechanical loading of these architectures show that the surface can be in a compressive stress state, following a short shakedown plasma exposure, thus mitigating surface fracture.

© 2016 Elsevier B.V. All rights reserved.

1. Introduction

Plasma-facing materials (PFM) are required for a great number of technological applications, encompassing space electric propulsion devices, micro-electronics fabrication, fusion energy conversion, and pulsed power devices, just to name a few. Continued development of space Electric Propulsion (EP), fusion energy, and Pulsed Power (PP) systems relies on fundamental advances in our understanding of material performance and survival in extraordinarily severe environments. The demand of higher performance materials is even greater in future technologies that will require materials to operate in substantially more aggressive environments. In such applications, PFM encounter unprecedented severe thermomechanical environments, as plasma ions and electrons slam onto the surface. Many physical degradation phenomena ensue, including material loss by ablation, blistering, sputtering and evaporation, as well as genuine thermoemchanical damage in the form of extensive plastic deformation and complex surface cracking.

To understand thermomechanical damage induced by intermittent high heat flux, one has to consider the main driver of damage accumulation, namely plastic deformation of some material regions that are constrained from expansion by cooler regions, or by external boundary conditions. Transient high heat flux induces a temperature gradient across PFM, which if constrained from bending or lateral expansion, can result in thermal stresses that exceed the yield point of the material. Considerations of cooling would require that a mechanical force, generated by the fluid pressure on the cold side, would also act on the PFM simultaneously with the thermal stress. While the mechanical force is generally constant, the thermal stress will fluctuate with each cycle, as the plasma heat source is turned on and off. Several interacting phenomena and manifestations of thermomechanical damage may take place under these specialized loading conditions; encompassing purely elastic response, shakedown behavior, reverse plasticity with ratcheting, viscoplastic deformation, and surface fracture. Considerations of the possibility of these outcomes, and finding solutions to mitigate the accumulation of

* Corresponding author.
E-mail address: ghoniem@ucla.edu (N.M. Ghoniem).

http://dx.doi.org/10.1016/j.jnucmat.2016.12.034
0022-3115/© 2016 Elsevier B.V. All rights reserved.

thermomechanical damage through materials design are desirable pursuits in the development of resilient PFM for many demanding applications. We review briefly here related research on these phenomena as motivating background for the present work. We will first discuss classical approaches of elasto-plasticity employed for the solution of this problem. Since these approaches will be shown to have serious limitations and approximations, we will then review more fundamental modeling strategies that are based on including microstructure information. A discussion of experimental testing methods will be given, followed by engineering design approaches that are used to mitigate thermomechanical damage effects.

Classical methods of elasto-plasticity were developed to describe cyclic plasticity, often based on assumptions of the constitutive behavior of the material in a thermomechanical environment. Structural models for the analysis of residual thermal stresses in structures falls into two main simplifications: (1) connected bars that expand/contract at different rates upon uniform heating; and (2) beam/membranes that are prevented from bending and are subject to a temperature gradient. For example, Parkes [1] studied the problem of thermal ratchetting in an aircraft wing, and assumed it to be a two-bar structure in which the temperature of one bar is cycled while the temperature of the other bar is kept constant. Jiang and Leckie [2] presented a method for direct determination of the steady solutions in shakedown analysis of the two-bar problem. On the other hand, Bree [3] analyzed the elastic-plastic behavior of a thin cylindrical tube subjected to constant internal pressure and cyclic temperature drop across the tube thickness. He used a simple one-dimensional model, assumed a constant temperature gradient across the tube thickness and an elastic-perfectly plastic constitutive model. Many other researchers expanded on the basic Bree model of cyclic plasticity by considering kinematic hardening [4], creep effects [5], and shakedown loads with hardening [6]. These considerations are based on the idea of neglecting the axial stress in internally pressurized thin tubes, and applying equilibrium conditions on hoop stresses. When one introduces an elastic-perfectly plastic material model, four main regimes of behavior arise during cyclic thermal loading. At low mechanical (pressure) and thermal stress ranges, elastic behavior is expected (E-regime). As the temperature gradient increases with little increase in the mechanical stress, the cross-section becomes fully plastic (P-regime). At high values of mechanical and thermal stresses, thin structures enter into a "ratcheting, or R-regime." At moderate values of both thermal and mechanical stresses, the structure undergoes shake-down for a few cycles and settles with elastic behavior thereafter. The details of these four possibilities have been worked out by Bree [3], and have been incorporated into high temperature design codes [7–9].

Despite the success of classical elasto-plasticity methods in design applications (e.g. the adoption of the Bree diagram by the ASME design code for high temperature components [7–9]), they are limited in describing severe plasma transient effects on PFM. For example, Bree's original analysis was based on an elastic perfectly plastic, one-dimensional stress model of residual stresses, where material properties are assumed not to change from cycle-to-cycle. However, high temperature deformation entails a variety of physical phenomena such as dislocation climb, recovery, recrystallization, and subgrain growth, in addition to traditional dislocation glide mechanisms accompanying plastic deformation. All of these mechanisms become active to varying degrees by the presence of an elevated temperature (typically $> 0.4\,T_m$), and lead to gradual changes in the constitutive behavior of the material as severe thermal cycles are applied to it. The lack of any physical input into the thermomechanics of high heat flux components casts doubt on the predictive qualities of classical model. For these reasons, physically-based approaches, where dislocations are modeled as the basic carriers of plastic deformation, can lead to greater insight into the nature of thermomechanical damage accumulation.

The primary aim of the visco-plastic formulation presented here is to describe the thermomechanical response of PFM on a physical basis, where the microstructure (dislocations and grains) is represented. Among the earliest of microstructure-based plasticity models is a formulation by Kocks and Mecking (KM - model) [10–12]. The KM - model assumes that the strain rate, temperature, and internal parameters such as dislocation density (ρ), all play a role in determining the flow stress. This, in turn, follows the well-known Taylor hardening relation, namely that $\sigma = s(\dot{\varepsilon}, T)\widehat{\alpha}\mu b\sqrt{\rho}$, where $s(\dot{\varepsilon}, T)$ is a rate sensitive function, $\widehat{\alpha}$ is a constant on the order of unity, and μ is the shear modulus. This flow stress depends only on the resistance to deformation offered by the presence of dislocations. Since hardening or softening can occur as a result of dislocation-dislocation interactions, both the hardening and recovery rates have to be modeled. The Taylor hardening relationship in the KM model is written as: $\sigma d\sigma/d\varepsilon = (\alpha\mu b)^2/2 \times d\rho/d\varepsilon$, where the dislocation density is assumed to be a function of the strain via a rate equation that balances dislocation production with further straining and its rate of recovery, as: $d\rho/d\varepsilon = (\Lambda b)^{-1} - L_r N_r \nu_r/\dot{\varepsilon}$. The first term in the equation describes the rate of dislocation storage; while the second is the dynamic recovery rate. Λ is the mean free path a dislocation travels before it is annihilated or ceases to contribute to the plastic flow of the material, it is assumed to be proportional to the dislocation spacing $1/\sqrt{\rho}$, L_r is the length of dislocation segments, N_r is the dislocation density, and ν_r is the rate at which the dislocations are rearranged. The glide kinetics of the model can be described with an Arrhenius equation of the form: $\dot{\varepsilon} = \dot{\varepsilon}_o \exp -\frac{\Delta G(s_A)}{kT}$. The activation energy for dislocation glide $\Delta G(s_A)$ is dependent on stress and is given by: $s \equiv \frac{\sigma}{\widehat{\sigma}} = \left(\frac{\dot{\varepsilon}}{\dot{\varepsilon}_o}\right)^{1/m}$, where $\widehat{\sigma}$ is the flow stress at 0 K, and m is the strain rate sensitivity.

Following similar lines to the KM approach, dislocation density based plasticity models have been advanced. Estrin et al. [13]. developed a model, which takes into account the cellular nature of the dislocation microstructure, and adequately described stages III, IV, and V of the stress-strain curve. Prinz and Argon similarly developed a framework by which stages III and IV of the stress-strain curve were accurately predicted [14]. Temporal dynamical behavior and spatial patterning have been analyzed with dislocation density models. Kubin and Estrin described the critical conditions for the Portevin-Le Chatelier effect [15], while the collective dynamical behavior of dislocations was investigated by Anan-thakrishna [16], and by Kubin, Fressengeas, and Ananthakrishna [17]. Spatial patterning of dislocations in ordered structures, such as dislocation cells and Persistent Slip Bands (PSB) has been modeled with dislocation density equations by Walgraef and Aifantis [18–20], and extensively by Aifantis [21]. On the other hand, Kamada and Zikry developed a 3-D dislocation-based model, and applied the model to the deformation of intermetallics [22], and the effects of grain boundaries on large-strain deformation was also studied [23]. Several applications of the model were extended to other material systems [24,25]. Arsenlis and Parks developed a dislocation-density based model to study the crystallographic aspects of geometrically-necessary and statistically-stored dislocation densities [26], and the evolution of crystallographic dislocation density in crystal plasticity [27].

It is interesting to note that despite the wide variety of dislocation-based models of plasticity [28], there have been relatively few formulations which explicitly incorporate high

temperature effects, such as creep and creep-fatigue interactions [29]. At elevated temperatures ($T > 0.5\ T_m$), additional elements must be included in a micro-structure-based model. The subgrain microstructure becomes the rate controlling mechanism, and details of subgrain boundaries (e.g. the dislocation spacing inside the subgrain boundary, misorientation angles, etc.) take on a more urgent importance. In fact, subgrain boundaries are considered the main source of the long-range internal backstress [30,31]. Additionally, plastic deformation is no longer controlled by dislocation glide, but is often described as *climb-controlled-glide*, where the effective slip rates are much slower glide rate at low-temperature thanks to the sluggish climb of dislocation cores in vacancy supersaturations.

In section 2, we present details our Ghoniem-Matthews-Amodeo (GMA)model [32], where it is re-formulated within the large deformation framework of the Finite Element Method (FEM) in subsection 2.1, and extended to modeling bcc polycrystals in subsection 2.2. Section 3 presents the results of FEM simulations based on the present GMA-poly model. First, the model is calibrated with a suitable set of parameters for the creep deformation of tungsten in subsection 3.1. This is followed by presenting results of simulations in a representative polycrestal in subsection 3.2. The model will be applied to our experimental results on micro pillars that have a composite structure, with a rhenium core and a thin tungsten coating [33] in subsection 3.3 for homogeneous plastic deformation of the W shell. Based on the insight gained from the microstructure-based crystal viscoelasticity model, we then present ideas on how to design a plasma-resilient surface with controlled micro-pillar architecture in subsection 3.4. Finally, conclusions of this study are given in section 4.

2. Dislocation-based crystal viscoplasticty

We have formulated a microstructure-based model that contains these critical elements necessary to describe high-temperature deformation [34]. In its original form, the Ghoniem-Matthews-Amodeo (GMA) model assumes that the material is homogeneous, and does not account for large-deformation kinematics that would be associated with creep-type deformation. Moreover, it does not explicitly account for the slip systems in each grain so as to model spatially non-homogeneous deformation. In this work, we will extend the GMA model within the framework of large-deformation crystal plasticity. The current extension of the model will be termed GMA-poly for brevity. The GMA model captures key high temperature deformation phenomena, such as recrystallization, subgrain nucleation and growth, static and dynamic recovery, in addition to the basic ingredients of dislocation storage and annihilation inherent in the KM model and all other variants [34]. The formulation is based on many developments in creep theory, such as the work by Nabarro [35], Gittus [36], Bullough et al. [37,38], Heald et al. [39], and Kassner [40]. Under these conditions, dislocation cells form and evolve into subgrains. The inclusion of the subgrain microstructure evolution is a key aspect of this model as reviewed in Refs. [41,42]. The GMA model is based on earlier developments and experimental observations by a number of investigators (Takeuchi et al. [43], Langdon [44], Challenger et al. [45], Michel et al. [46], and Cuddy [47]).

2.1. Large-deformation FEM crystal plasticity framework

The purpose of the GMA model is to compute shear strain rates in slip systems from knowledge of dislocation densities, as will be presented in subsection 2.2. It is incorporated into a crystal plasticity framework with large deformation by recognizing the key connection between physics (shear rates from dislocation densities) and mechanics (displacements and stresses). First, the plastic velocity gradient tensor, $\mathbf{L}^p$, is computed by summing up the shear strain rates ($\dot{\gamma}_\alpha$) on all slip systems (α), described by the slip vector ($\mathbf{s}^\alpha$) and the plane normal ($\mathbf{n}^\alpha$). Thus, $\mathbf{L}^p = \sum_{\alpha=1}^{m} \dot{\gamma}_\alpha \mathbf{s}^{(\alpha)} \otimes \mathbf{n}^{(\alpha)}$.

The increment of deformation in a crystal is assumed to take place by a multiplicative decomposition of the total deformation gradient tensor into an elastic and a plastic component: $\mathbf{F} = \mathbf{F}^e \cdot \mathbf{F}^p$. The total deformation gradient is determined from the displacement vector field, as: $\mathbf{F} = \nabla \mathbf{u} + \mathbf{I}$, where $\mathbf{u}$ is the displacement vector, and $\mathbf{I}$ is the identity matrix. The deformation mapping is assumed to start from a reference state to an intermediate state by simple shear deformation on slip systems. This is followed by elastic lattice deformation from the intermediate to current current configuration.

The shear strain rate $\dot{\gamma}$ is calculated by solving a system of ODEs representing various dislocation densities, as well as an evolution equation for the subgrain radius, as will be described in the next subsection. By distributing the ODE's constituting the structure of the GMA model over a computational grid provided by an FE mesh, the shear strain rate $\dot{\gamma}$ can be computed in every element. Upon finding the shear strain rate from GMA model, the components of the velocity gradient can in turn be found by a similar process in which the system of ODE's is solved point-wise over an FE mesh. For rate-dependent plastic deformation gradient tensor, $\mathbf{F}^p$ is updated with the following space-dependent equation, once the components of the velocity gradient are known: $\dot{\mathbf{F}}^{\mathbf{p}} = \mathbf{L}^p \cdot \mathbf{F}^p$. The assumption of multiplicative decomposition of the elastic and plastic deformation gradient tensors is then utilized to calculate $\mathbf{F}^e$, which is necessary to determine the stress state. A potential energy functional, Π can be expressed as:

$$\Pi = \int_{B_0} \tilde{w}(\mathbf{E}^{\mathbf{e}}) J^p d\Omega_0 - \oint_{\partial B_0} t_i u_i dS_0 \tag{1}$$

where $\tilde{w}$ is the strain energy density per unit intermediate volume and J^p is the determinant of $\mathbf{F}^p$. The relationship between volumes in the intermediate and reference configurations: $J^p d\Omega_0 = d\tilde{\Omega}$ has been used. Based on the minimum total potential energy principle, the displacement field minimizes the potential energy with a given $\mathbf{F}^p$. The first variation of Π with respect to an arbitrary change in $\mathbf{u}$ vanishes, which gives the following weak form of the equilibrium equation:

$$\delta\Pi = \int_{B_0} P_{iJ} \delta u_{i,J} d\Omega_0 - \oint_{\partial B_0} t_i \delta u_i dS_0 = 0 \quad \forall \delta \mathbf{u} \tag{2}$$

where the first Piola stress $\mathbf{P}$ is given in terms of the second intermediate stress $\mathbf{W}$ and can be expressed as $P_{iJ} = W_{\alpha\beta} F^e_{i\alpha} G^p_{J\beta} J^p$. Assuming that the strain energy density is quadratic in the elastic strain, $\mathbf{W}$ can be expressed as $W_{\alpha\beta} = \frac{\partial \tilde{w}}{\partial E^e_{\alpha\beta}} = \lambda E^e_{\gamma\gamma} \delta_{\alpha\beta} + 2\mu E^e_{\alpha\beta}$. Equation (2) is the weak formulation of the large deformation problem, which can be implemented within the FEM framework. The computational scheme is schematically shown in Fig. 1.

2.2. Polycrystalline GMA viscoplasticity model

In low-temperature plasticity models, the flow stress is generally dictated by the dislocation density, with additional contributions from the grain size (the Hall-Petch effect). Hence, efforts to develop strong materials are focused on grain refinement and nano-crystalline materials. However, at elevated temperatures, grain growth takes place, and individual grains subjected to an

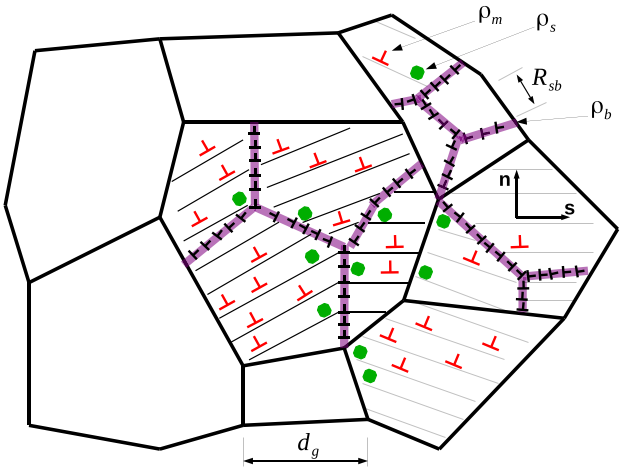

Fig. 1. Sketch of the main features of the GMA model. Each grain has a diameter d_g, is subdivided into subgrains, each of which has a radius R_{sb}. Within each grain, three dislocation groups are present: forest with density ρ_s, mobile with density ρ_m, and boundary dislocations of density ρ_b.

applied stress for prolonged periods start to subdivide themselves naturally into subgrains of a size that is inversely proportional to the applied stress [42]. This behavior is so unusual, and when modeling high temperature deformation, one must then account for the nucleation and growth of such subgrains. The is because the role of the original grain boundaries in controlling the creep resistance is replaced with that of subboundaries. The various dislocation processes that take place at elevated temperatures are discussed by Gittus [48], Li [49], and Sandström [50,51], and can be summarized as: multiplication of dislocations within the subgrains., annihilation of mobile dislocations within the subgrains, annihilation of dislocations at the subgrain walls, absorption of dislocations by the subgrain walls, emission of dislocations by the subgrain walls, nucleation of new subgrains, and growth of subgrains by coalescence.

In this polycrystalline development of the GMA model, we consider each grain to have a number of slip systems, each of which (α) is described by a vector diad, **s** and **n** for the slip direction and normal, respectively. Each grain has a grain diameter, d_g, and is further subdivided into subgrains. Thus, on average, only a set of slip systems is considered for each grain because misorientations between subgrains are small, as can be seen schematically in Fig. 1. The average sub grain radius is R_{sb}, which can grow to reduce the stored elastic energy, or shrink due to nucleation of fresh subgrains during deformation. The dislocation population is divided into three interaction groups, distinguished by their average speed. Mobile dislocations have a density of ρ_m and those can glide causing plastic deformation. Forest or *static* dislocations do not move and they obstruct the motion of mobile dislocations resulting in hardening. Finally, near sub boundaries, dislocations align to enter or leave the sub boundary; they move slowly by climb, and their density is ρ_b. The sketch in Fig. 1 shows the elements of the conceptual model, originally presented in Ref. [34].

While the original presentation of the GMA model can be found in Ref. [34], we further expand this model here, incorporating a number of novel features. These are: (1) extension to multi-slip crystals; (2) an update of the dislocation mobility law with a more comprehensive formulation for bcc metals [52]; (3) incorporation of the model into a large-deformation FEM framework, as discussed in the previous subsection; and (4) applications in the design of high heat flux resistant materials. We give here a concise description of the original model, and then extend it to the large-deformation of polycrystals.

The GMA model develops conservation equations using rate processes for the three main dislocation populations on each slip system, $\rho_m^{(\alpha)}, \rho_s^{(\alpha)}, \rho_b^{(\alpha)}$, for mobile, static, and boundary dislocations, respectively. The rates are assumed to change by frequencies that are determined by basic glide, climb, or annihilation rates. Subgrains provide a source of mobile dislocations, and also act as barriers for mobile dislocations. The rate of mobile dislocation production within subgrains is the frequency of source operation times the source density. The frequency of source operation is $(\rho_m^{(\alpha)})^{1/2} v_g$, where $(\rho_m^{(\alpha)})^{1/2}$ is the reciprocal of the mean free path of mobile dislocations in slip system α. Thus, the rate of change of the mobile dislocation density as a result of mobile source operation is $(\rho_m^{(\alpha)})^{3/2} v_g$. Another dislocation source is the activation of links within the static dislocation population, which contributes to the growth of mobile dislocation line length. The frequency of static source activation is $v_g^{(\alpha)}/h$, where h is the dislocation spacing within the subgrains, and each time a source is activated, its length expands from h to R_{sb}, where is the subgrain radius. Thus, the frequency of line length production is $(v_g^{(\alpha)}/h) \times \frac{R_{sb}}{h}$, and the rate of change of the mobile dislocation density from this source is $\beta \rho_s^{(\alpha)} R_{sb} v_g / h^2$, where β is a geometry fitting factor. The dislocation spacing within the wall, h can be written as: $h = \frac{1}{(\rho_s + \rho_b) R_{sb}}$. On the other hand, the frequency of immobilization is $v_g^{(\alpha)}/(2R_{sb})$, since dislocations travel across the sub grain diameter before they are immobilized. Thus, the rate of immobilization is $\rho_m^{(\alpha)} v_g/(2R_{sb})$. Other rates have been derived in Ref. [34]. The rate of mobile dislocation recovery by climb is $8 v_{cm} \rho_m^{(\alpha)}$, and the rate of dynamic recovery is $\delta v_g^{(\alpha)} \rho_m^{(\alpha)} (\rho_m^{(\alpha)} + \rho_s^{(\alpha)})$, where v_{cm} is the mobile dislocation climb velocity, and δ is the average distance between annihilating dislocations.

These glide-controlled rates are complemented by static and dynamic recovery rates. The phenomenon of dislocation climb contributes to the static recovery rate, and proceeds by the climb of dislocation dipoles into the subgrains. The effective stress that the dislocation dipoles exert on each other can be expressed as: $\sigma_c = \mu b / 2\pi(1-\nu)s$, where s is the separation distance between the dipoles. The climb-to-mutual annihilation of a dipole with initial separation s_0 is shown to be $\tau \simeq \frac{s_0}{4 v_c}$ [34], where the initial dipole separation is $s_0 = \rho_m^{-1/2}$. Thus, the recovery rate of mobile dislocations is $-\frac{2\rho_m}{\tau} = -8\rho_m^{3/2} v_{cm}$. Likewise, the forest dislocation recovery rate can be expressed as $-\frac{2\rho_s}{\tau} = -8\rho_s \frac{v_{cs}}{h}$, where the initial dipole separation is $s_0 = h$. The flux of vacancies along the dislocation core can be expressed as [53].

$$j_p = 2 D_p \sigma_c^{(\alpha)} \Omega / L_p kT \tag{3}$$

where D_p is the core diffusion coefficient, and L_p is the path length for diffusion along core, Ω the atomic volume, and $\sigma_c^{(\alpha)}$ is the climb component of the stress tensor in slip system α. The climb velocity is then

$$v_c^{(\alpha)} = 2\pi b D_p \sigma_c^{(\alpha)} \Omega \Big/ L_p^2 kT \tag{4}$$

Dynamic recovery explains the saturation of strain hardening [54], because it assumes that mobile dislocations of opposite sign would annihilate each other over time. This was first recognized by Johnson and Gilman [55], and Webster [56], and can be expressed by the following recovery rate: $-\delta \rho_m^{(\alpha)} (\rho_m^{(\alpha)} + \rho_s^{(\alpha)}) v_g$, where δ is an

average distance between dislocations characterizing annihilations [38,57]. The grain boundary evolution can be modeled as the product of driving pressure and mobility [34].

The sub-boundary energy per unit area, γ_{sb} for low-angle subgrain boundary can be expressed as: $\gamma_{sb} \simeq \frac{2\mu b^2}{3}\rho_b^{(\alpha)} R_{sb}$. Since, the subgrain grows by boundary coalescing of collapsing small subgrains, the total force acting on a boundary for a collapsing subgrain (the Gibb's Thompson driving force, $\frac{2\gamma_{sb}}{R_{sb}}$) can be written as: $P_{sb} \simeq (4/3)\mu b^2 \rho_b$, and the growth rate of a sugrain is simply the product of the sub grain mobility and the driving force, $\partial R_{sb}/\partial t = M_{sb}(P_{sb} - 2\pi r_p^2 N_p \gamma_{sb})$, where the effects of any precipitates (density N_p and radius r_p) is taken to oppose the driving Gibbs-Thompson force. Sugrains are assumed to nucleate when the total density exceeds a critical value. It is assumed that the driving force for nucleation has the form $\mu b(\rho_\alpha^{1/2} - K_c/2R_{sb})$, where ρ_α is the sum of the mobile and forest dislocation densities in slip system α. K_c is a constant on the order of 10 [58,59]. The time to nucleate a new subgrain configuration is expressed as: $\tau = (kT/\mu\eta_v K_c \rho^{1/2} D_s)[\rho^{1/2} - (K_c/2R_{sb})]\Omega$. The above expressions can be combined to obtain the following rate equation for subgrain radius.

$$\frac{dR_{sb}}{dt} = -\mu\eta_v K_c R_{sb}\left[\rho^{1/2} - (K_c/2R_{sb})\right]^2 \Omega D_s/kT \tag{5}$$

Equation (5) is only applicable when there is a driving force for nucleation, i.e. $\rho^{1/2} > K_c/2R_{sb}$. The total dislocation density in the grain is $\rho = \sum_{\alpha=1}^{N}(\rho_m^{(\alpha)} + \rho_s^{(\alpha)})$.

The summary presented above requires knowledge of the glide velocity, which is one of the most significant ingredients in the GMA formalism. Because the model is an effective phenomenological procedure, the resolved shear stress on a glide plane is assumed to be resisted by a friction stress that takes into account the effects of solute atoms on dislocation motion. The internal stress must thus be analyzed, since the effective stress, which is a function of internal stress, will be incorporated in the formulation of dislocation velocity. The internal stress is caused by any opposition to dislocation motions, and this opposition can be characterized into three sources. The first source is any precipitates and other dislocations that oppose dislocation motions. The internal stress that mobile dislocations must overcome is $\mu b/2\pi\lambda$, where λ is the effective obstacle spacing, and μ is the shear modulus. In the case where both precipitate and dislocation obstacles are present, the effective obstacle spacing λ is given as

$$\lambda = 1/(1/\lambda_d + 1/\lambda_p) \tag{6}$$

λ_d is the inter-dislocation spacing, and is given as $\lambda_d = 1/\rho_m^{1/2}$. λ_p is the inter-precipitate spacing, and is given as $\lambda_p = 1/(N_p r_p)^{1/2}$, where N_p is the volume concentration of precipitates, and r_p is the mean radius. The second source of opposition are the dislocations that have not yet neutralized their long-range stress fields. Essentially these dislocations have not moved into their low-energy configuration. The mobile dislocations could be accelerated or retarded depending on the nature of these un-neutralized stress fields. These unstable dislocations are forest dislocations within the subgrains. The boundary dislocations themselves do not contribute to the internal stress beyond a distance greater than the average dislocation distance within the subgrains [60]. Combining the effects of precipitates and unstable forest dislocations, the long-range internal stress can be expressed as

$$\tau_i^{(\alpha)} = \mu b/2\pi\lambda + \zeta\mu b\left(\rho_s^{(\alpha)}\right)^{1/2} \tag{7}$$

The third source of opposition is the friction resistance to glide from over-sized solutes. These typically are solute particles used to strengthen metals. For well-annealed materials without hardening precipitates and heat treatment, this stress can be identified as the initial flow stress, τ_0. Therefore, the resolved effective stress, τ_e can be represented as the following, where $\tau_{a,\alpha}$ is the applied shear stress component on slip system α.

$$\tau_e^{(\alpha)} = \tau_a^{(\alpha)} - \tau_i^{(\alpha)} - \tau_0^{(\alpha)} \tag{8}$$

A comprehensive phenomenological dislocation mobility law for the glide velocity in bcc metals has been recently developed by us [52]. The mobility law is based on fundamental theory of kink-pair controlled motion in the low temperature regime, and on phonon drag limited motion at high temperatures. The general form of the dislocation velocity (edge or screw) is given as [52]:

$$v_g^{(\alpha)}(\boldsymbol{\sigma}, T) = \begin{cases} \dfrac{\tau_{e,\alpha} b}{B(\boldsymbol{\sigma}, T)} \exp\left(-\dfrac{\Delta G_{kp}(\boldsymbol{\sigma}, T)}{2k_B T}\right) & \text{if } \Delta G_{kp}(\boldsymbol{\sigma}, T) > 0 \\ \dfrac{\tau b}{B(\boldsymbol{\sigma}, T)} & \text{if } \Delta G_{kp}(\boldsymbol{\sigma}, T) \le 0 \end{cases} \tag{9}$$

In Eq. (9), the free energy of kink-pair nucleation is ΔG_{kp}, such that $\Delta G_{kp} > 0$ defines the regime of active kink-pair mechanism. The function $B(\boldsymbol{\sigma}, T)$ is a phonon drag coefficient, determined from atomistic simulations [52], and is a function of the temperature and the entire stress tensor, $\boldsymbol{\sigma}$. The kink-pair nucleation energy ΔG_{kp} is also a function of temperature and the stress tensor, and allows manifestations of key aspects of plastic deformation in bcc metals (e.g. W), such as the tension-compression asymmetry, and the twinning-anti-twinning asymmetry [52]. $\tau_{e,\alpha}$ is the resolved shear stress on slip system α. For the purposes of the present studies of creep deformation of tungsten at high temperature, we adopt a simplified version of the mobility law, given by:

$$v_g^{(\alpha)} = \frac{a_1 \tau_e^{(\alpha)} \Omega}{kT} \exp\left(\frac{-\Delta G_g}{kT}\right) \tag{10}$$

where a_1 and ΔG_g are fitting parameters.

The overall model is comprised of three conservation equations for the dislocation densities, and one rate equation for the average size (radius) of the subgrain. These are given by:

$$\frac{d\rho_m^{(\alpha)}}{dt} = v_{g,\alpha}\left(\rho_m^{(\alpha)}\right)^{3/2} + v_{g,\alpha}\beta R_{sb}\rho_s^{(\alpha)}\Big/h^2 - v_{g,\alpha}\rho_m^{(\alpha)}\Big/(2R_{sb}) \tag{11}$$

$$-8\left(\rho_m^{(\alpha)}\right)^{3/2} v_{cm} - \delta\rho_m\left(\rho_m^{(\alpha)} + \rho_s^{(\alpha)}\right) v_{g,\alpha} \tag{12}$$

$$\frac{d\rho_s^{(\alpha)}}{dt} = v_{g,\alpha}\rho_m^{(\alpha)}\Big/(2R_{sb}) - 8\rho_s^{(\alpha)} v_{cs}/h - \delta v_{g,\alpha}\rho_m^{(\alpha)}\rho_s^{(\alpha)} \tag{13}$$

$$\frac{d\rho_b^{(\alpha)}}{dt} = 8(1-2\zeta)\rho_s^{(\alpha)}\frac{v_c}{h} - \left(\frac{\rho_b^{(\alpha)}}{R_{sb}}\right) M_{sb}\left(p_s - 2\pi r_p^2 N_p \gamma_{sb}\right) \tag{14}$$

$$\frac{dR_{sb}}{dt} = M_{sb}\left(p_s - 2\pi r_p^2 N_p \gamma_{sb}\right) - \mu\eta_v K_c R_{sb}\left[\rho^{1/2} - \frac{K_c}{2R_{sb}}\right]\frac{\Omega D_s}{kT} \tag{15}$$

The shear strain rate in slip system α is finally given by the Orowan–Baily relationship, which is needed to solve for the velocity gradient tensor within the FE framework described in the previous subsection.

$$\frac{d\gamma_\alpha}{dt} = b\rho_m^{(\alpha)} v_g^{(\alpha)} \tag{16}$$

The first three conservation equations balance production (source) and annihilation rates. For $\rho_m^{(\alpha)}$, the first and second terms are the production rates from the mobile population and sub grain walls, respectively, the third is for annihilation at sub grain walls, the fourth is for climb recovery, and the last is for dynamic recovery. For $\rho_s^{(\alpha)}$, the first term is for immobilization at sub grain walls, the second is for climb recovery, and the last is for dynamic recovery. For $\rho_b^{(\alpha)}$, the first term is the production rate from static dislocations incoming into the boundary, the second is for annihilation of boundary dislocations by the creation of new sub grain surface. Finally, the rate equation for the sub grain radius is a balance between the growth rate by reduction of surface area, and the second is the rate of annihilation by creation of new sub grain surface.

3. Results

3.1. Model calibration

The extended GMA model was first calibrated to obtain the best possible fitting parameters for the creep response of tungsten at high temperature. The results of the fitting procedure are shown in Fig. 2, together with experimental data at 1600 °C taken from Ref. [61]. The optimized set of fitting parameters are listed in Table 1. The values of the atomic volume and magnitude of the Burgers vector were taken as $\Omega = 1.58 \times 10^{-29}$ m^3, and 0.274 nm, respectively. The current set of parameters listed in Table 1 reproduce the experimental data for the transient and steady state regime of tungsten creep at 1600 °C, and show that as the temperature is increased further, the creep rate increases significantly, as observed experimentally [61]. It is worth mentioning that a more extensive fitting procedure for creep strain as a function of temperature and stress has been previously achieved for the ferritic steel HT-9 in Ref. [34].

3.2. Modeling polycrystalline materials

To demonstrate the feasibility of the computational algorithm discussed in section 2, a simplified polycrystal model will be presented as an example. A five-grain tungsten polycrystal disc of diameter 0.6 μm and height of 0.16 μm, as shown in Fig. 3, is subjected to a tensile strain rate of 0.02 s^{-1}. The top surface was allowed to move only in the z-direction, while the bottom surface was constrained to move only in x and y directions. For simplicity, only one slip system in each grain was considered, as shown in Fig. 3. Detailed slip directions and slip plane normals are listed in Table 2 (see Fig. 3-b).

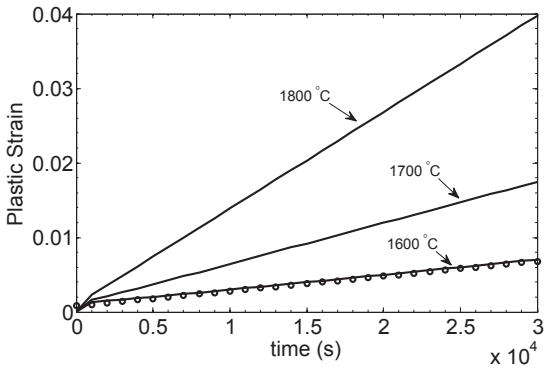

Fig. 2. Model calibration results using fitting parameters given in Table 1, experimental data (open circles) at 1600 °C taken from Robinson and Sherby [61].

Table 1
Fitting parameters used in the viscoplasticity model for W.1.

Parameter	Value	Unit	Description
β	1×10^4	–	Source density parameter
a_1	170	m s^{-1}	phonon drag parameter
ζ	0.2	–	static-to-boundary fraction
X_{jog}	0.0455	–	Jog fraction
D_0	1×10^{-11}	m^2 s^{-1} [61]	Diffusion pre-exponential
E_{self}	5.95	eV [61]	Self diffusion energy
Q	18.2	Ω[62]	Activation Volume
ΔG_g	3.18	eV	Glide activation energy

The simulations were carried out at 1600 °C, with the GMA fitting parameters obtained in subsection 2.2. All equations, including the ODEs in the GMA model and the weak form of the equilibrium Equation (2) were solved in the commercial COMSOL software.

The spatial distribution of the Cauchy stress in z-direction (σ_{zz}) in the deformed configuration is shown in Fig. 4. Stress concentrations can be observed near the grain boundaries of different grains. This observation matches well with expectations, based on the orientations of assigned slip systems in the five grains. The stress-strain curves are plotted at one representative point inside each grain, as shown in Fig. 5. It is interesting to note in this illustrative example that the stress field is quite inhomogeneous, and that stresses vary from grain to grain by almost a factor of 2 at a strain of ≈ 4%.

3.3. Viscoplastic response to cyclic thermal loading

The developed model has been further integrated into a multiphysics framework, where a transient heat conduction problem is coupled with the GMA-poly elastic-viscoplastic model. In this section, we present results of the multi physics model, assuming that tungsten behaves as a homogeneous elasto-viscoplastic material, ignoring the grain structure in the thin W coating around the rhenium core. We also assume that the rhenium core of the pillars behaves elastically. The thin tungsten layer did not exhibit a clear polycrystalline structure (see Ref. [33]), while the stress range of the rhenium core in micropillars did not exceed its yield point. First, simulations were carried out for flat samples with a smooth W surface, which is exposed to repeated heating/cooling plasma cycles. To contrast the mechanical behavior, additional simulations were carried out for just one micro-pillar, with all the details of coupling transient heat conduction with elasticity in the interior core of the pillar (Re) and elasto-viscoplasticity for the W coating.

The plasma-exposed samples are 2″ diameter substrates made of molybdenum upon which W armor can be deposited. The flange is chosen to be made of this material as well in order to minimize the thermal stresses associated with testing at high temperatures. The samples must also be machined to allow for six taped (10–32) holes in order to secure the samples to the flange without leaking. The samples themselves have a cup-like structure in order to thin the layer being impacted with the heat flux sufficiently to generate a temperature gradient across the thickness of the sample. A three dimensional, rear, and cross sectional view of the sample geometry can be seen in Fig. 6-(a), (b), and (c) respectively. The sample is 1″

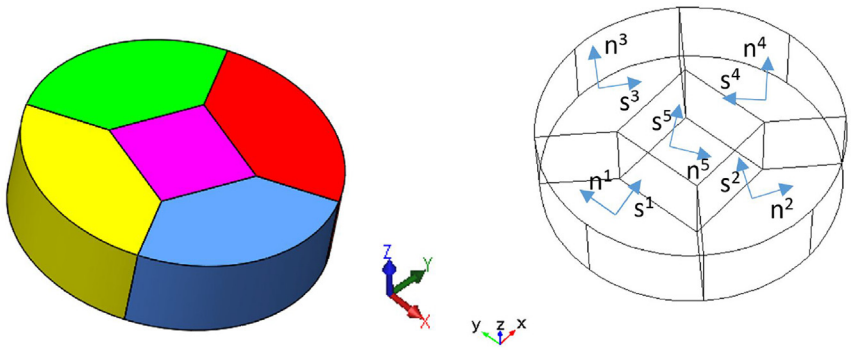

Fig. 3. Five-grain tungsten polycrystal model.

Table 2
Slip system orientations.

Slip system No.	Slip directions	Slip plane
1	[111]	[$\bar{1}$ 01]
2	[$\bar{1}$ 11]	[0$\bar{1}$ 1]
3	[$\bar{1}\bar{1}$ 1]	[011]
4	[$\bar{1}$ 11]	[101]
5	[111]	[0$\bar{1}$ 1]

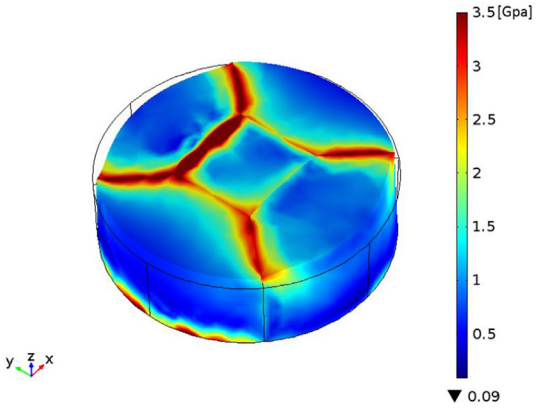

Fig. 4. Von-mises stress distributions in 5 W grains. Note the severe stress concentrations at grain boundaries.

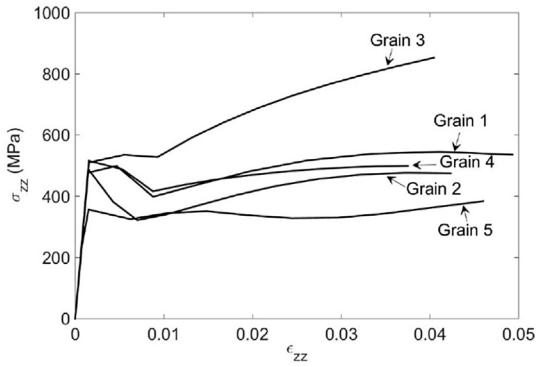

Fig. 5. Stress-strain curves in the five tungsten grains. Note the strong variation of the stress-strain response, with the stress in grain 3 being more than twice the stress in other grains.

thick and the pocket or cup is machined to be offset 3 mm from the surface, in essence the heat flux is impinging upon a 3 mm thick surface being cooled on the back end.

The back side of the sample is water cooled, and the cooling rate is controlled through the coolant velocity. The back side boundary condition has been set to simulate convective cooling, with the heat transfer coefficient being the control parameter. Typical simulation results for the surface stress ($h = 3$ kW m^{-2} K^{-1}) are shown in Fig. 7, where the color map is for the hoop stress at different times during a plasma exposure thermal cycle. It is seen that the hoop stress reverses from compressive to tensile, and by the end of the cool-down phase of the plasma cycle, it stays around 2 GPa. Such high tensile stress can explain our experimental findings reported in Ref. [33] that, for low rates of cooling, the sample fractures after only a few cycles of plasma exposure. The fracture toughness of polycrystalline W is high at temperatures above 800 °C (around 100 MPa$\sqrt{m}$), but falls sharply to less that 20 MPa$\sqrt{m}$ as the temperature decreases below 400 °C [63]. The dependence of the maximum surface hoop stress on the water cooling rate is shown in Fig. 8. As the water cooling rate is increased, the maximum compressive hoop stress is delayed during the cycle on-time, and its value decreases. It is clear that as the sample is cooled more vigorously, the residual plastic strain becomes small, and that the sample does not have significant locked-in residual stresses at the end of the plasma cycle. This is also what we observed in our experiments reported in Ref. [33]. The critical value of the heat transfer coefficient is found to be around 6 kW m^{-2} K^{-1}. Below this value, tensile stresses develop during the cool-down cycle, resulting in surface fracture.

The next set of simulations were conducted for micro-pillars that form the protective layer on top of the sample substrate. The micro-pillars were modeled as a 2 μm radius Re cylindrical core covered with a tapered W coat ranging in thickness from 0.5 μm at the thinnest point to 3 μm at the thickest point (base of the column), the pillar is 35 μm in height. An illustration of the pillars can be seen in Fig. 9, where the residual stress distribution at 43 s (radial stress in Fig. 9, and tangential in Fig. 9) is displayed as a color map. An incoming heat flux boundary condition was applied to the top of the pillar, while the bottom is modeled as connected to a semi-infinite solid. Adiabatic surfaces are assumed for the remaining boundaries as the vast majority of heat flow will enter and exit through the top and bottom of the micropillar, respectively. The micropillar is subjected to 6 pulses at a heat flux of 27 MW m^{-2} ($T_{on} = 5$ s, $T_{off} = 2$ s). The residual tangential and radial stresses are on the order of 1.3 GPa at the thinnest point of the W coating (towards the top of the pillar). Such a stress state could still be survivable without fracture given the small scale of the coating,

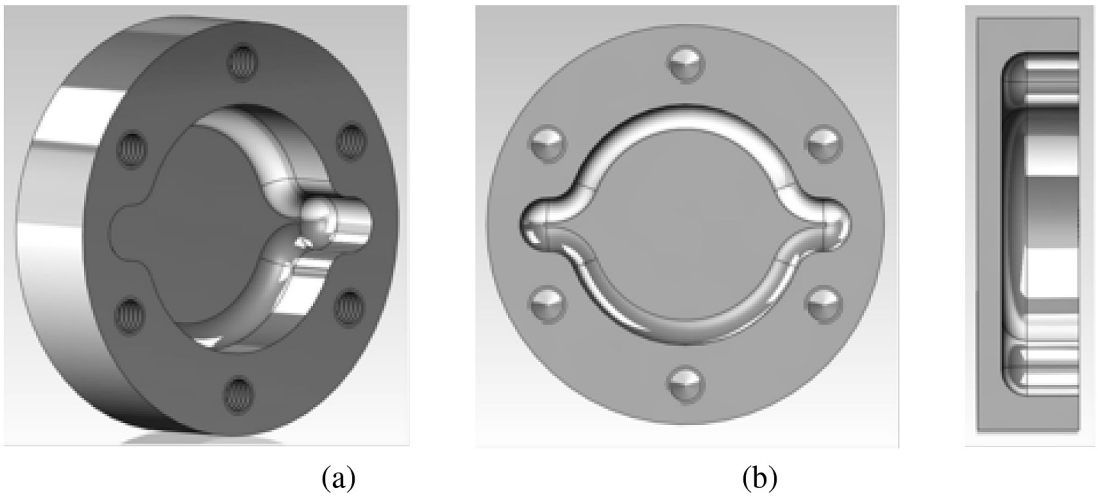

Fig. 6. Sample geometry (a) 3D view of sample showing back pocket (b) Rear view of sample, the six small holes on the perimeter are threaded in order to attach the sample to the flange, samples are 2″ in diameter (c) Cross sectional view of sample, thickness is 0.5″ and 0.118″ at the thinnest point.

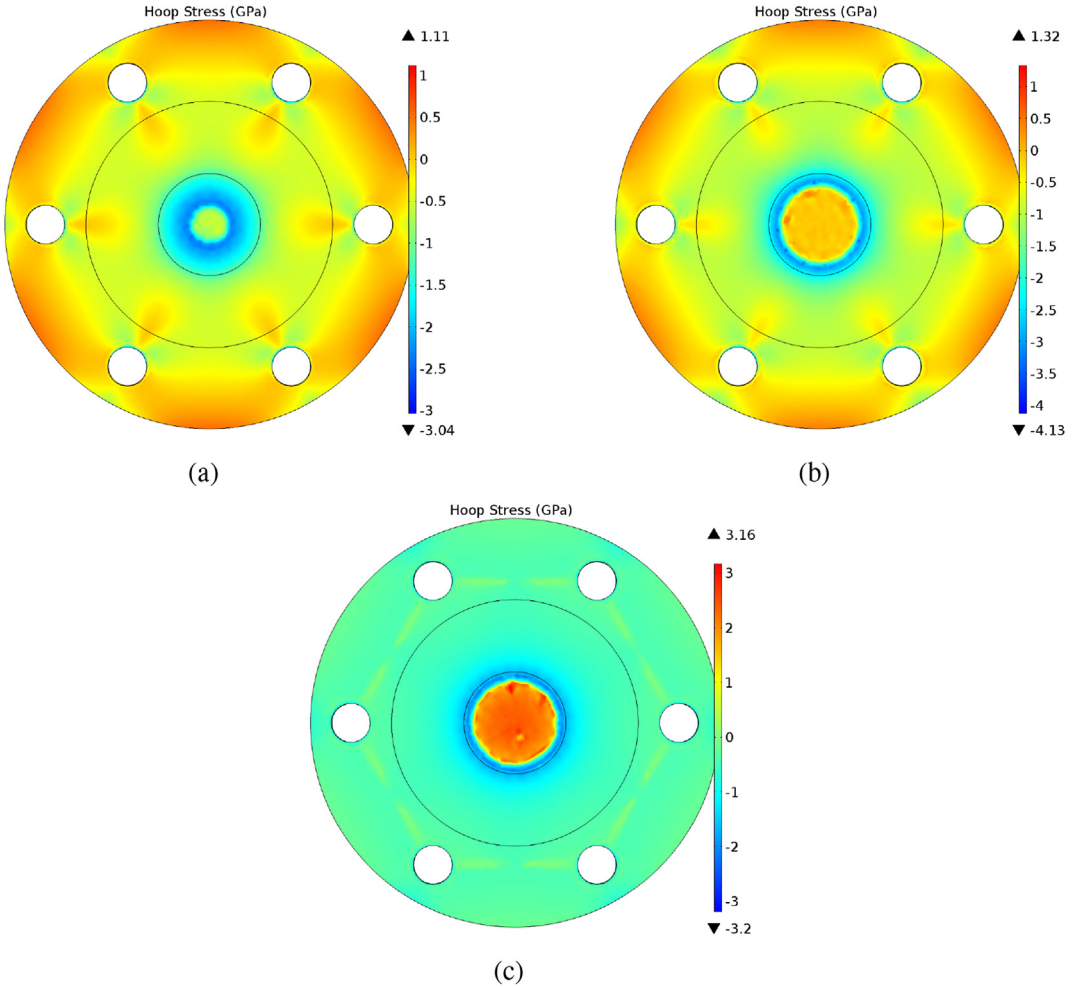

Fig. 7. Hoop stress distribution during a plasma exposure cycle (T_{on} = 5 s, T_{off} = 5 s), for h = 3 kW m^{-2} K^{-1} . Stress distribution at 2 s at 6 s, residual stress at 9 s.

however thermal fatigue would likely lead to fracture of the W coating in an extended thermal cycling environment, as was experimentally observed in Ref. [33].

The contrast in the stress response of a micro-pillar relative to a conventional (planar) surface can be observed in Fig. 10 for a 27 MW m^{-2} heat flux of 5 s duration. It is interesting to see that while the confinement of the cooler parts of the smooth surface sample causes high compressive stresses during the heat up phase,

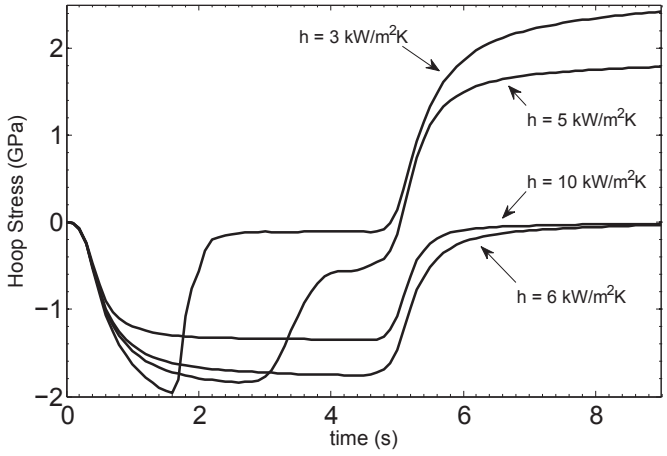

Fig. 8. The influence of cooling on the development of residual stresses at the end of a plasma heat cycle. The maximum hoop stress is shown as a function of time for various values of the heat transfer coefficient, h.

followed by high tensile residual stresses during cool-down, the micro-pillar behavior is quite the opposite. The rhenium core expansion during the heating part of the cycle puts the outer tungsten shell into tension, and residual stresses are relieved during the cool-down phase. The plastic strain plotted in Fig. 10 shows that, while larger plastic strains accumulate at higher heat flux levels, samples with flat smooth surfaces clearly retain higher levels of plastic strain, as compared to micropillars. Tapering of the pillars appears to be helpful in that residual plastic strain is reduced even further. This can be understood on geometric grounds, since thicker tapered W shells distribute the tensile stress caused by the expansion of the inner Re core.

Further changes in the geometry of the pillar can be shown to impact the stress response of the feature. The stress profile during a thermal pulse for a tapered and non-tapered micro-pillar is presented in Fig. 11. The stress evolution for these slightly different geometries is similar but for the fact that the non-tapered variant was exposed to a much smaller heat flux of 19 MW/m^2 relative to the tapered counterpart in which a 27 MW/m^2 pulse was applied. Both pillar varieties experience tensile tangential stresses at the

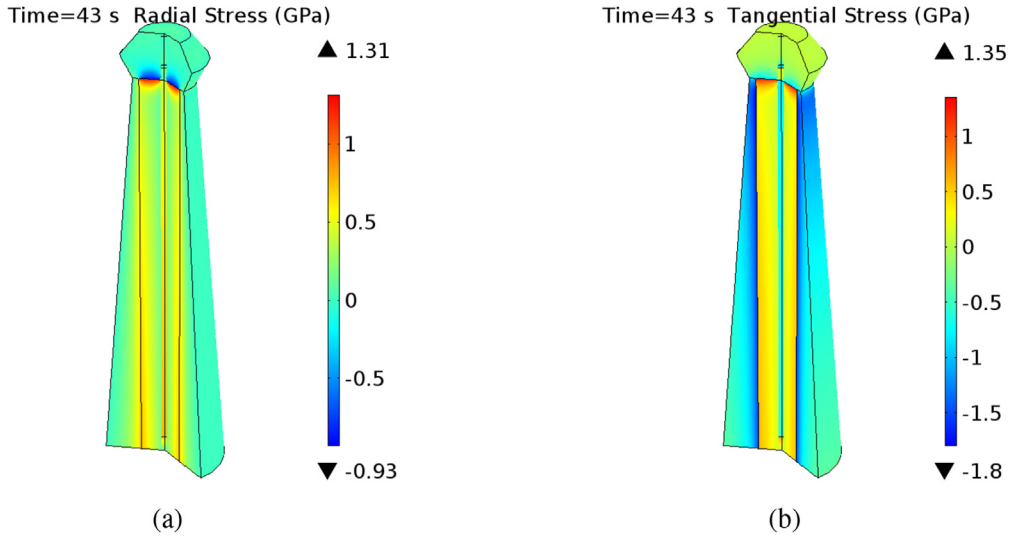

Fig. 9. Color maps of the radial and tangential stresses in a micropillar at the end of 6 plasma cycles. The heat flux is 27 MW m^{-2} (T_{on} = 5 s, T_{off} = 2 s). Note that the pillar is constructed of a Re pillar core with a W coating residual tangential stress. residual radial stress.

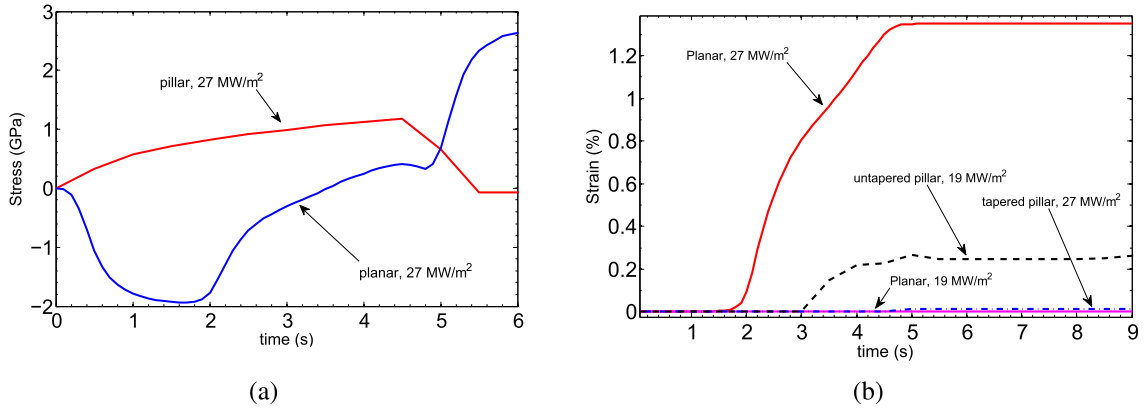

Fig. 10. Tangential stress in a sample with a smooth planar surface compared to a sample with a W-Re pillar during a 5 s pulse at a heat flux of 27 MW m^{-2}. Plastic strain in a smooth planar sample, tapered, and non-tapered W-Re micro-pillars, respectively, after one 5 s pulse.

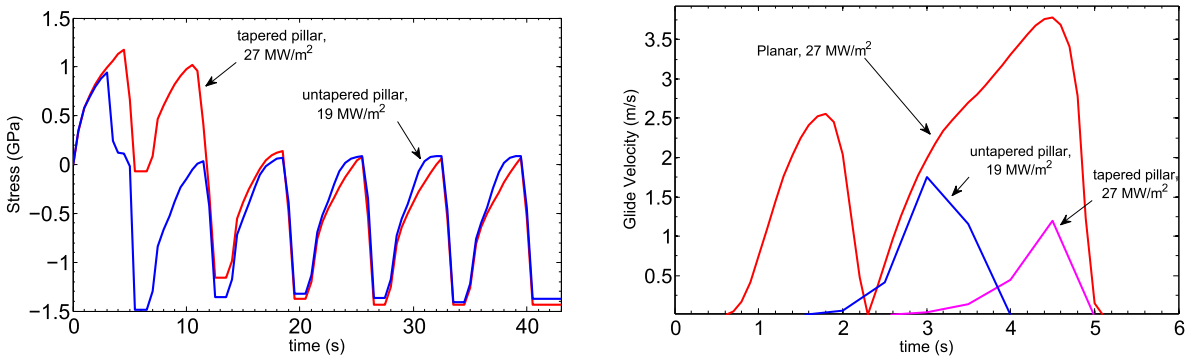

Fig. 11. Applied heat flux of 27 MW/m^2 Tangential stress in the W-Re pillar during a series of six 5 s pulses, note the material is pre-stressed during the initial pulse glide velocity in both high heat flux (HHF) sample and W-Re pillar during a 5 s pulse.

onset of the heat trial as would be expected from the larger expansion of the Re core, subsequent pulses however indicate that the W coat falls into a state of compressive residual stress. This compression stems from the contraction of the Re core upon cool-down of the pillar. The W coating is plastically deformed (expanded) under the aggressive Re pillar expansion during the first two thermal cycles, as the pillar cools the Re core attempts to contract back to its original dimension, in doing so it places the permanently enlarged W coat surrounding it into a state of compression. This thermomechanical condition amounts to placing the W coating under a state of pre-stress, all ensuing thermal pulses will have the effect of unloading the micro-feature from this residual stress. This demonstrates that a minor change in geometry can reduce the stress state and suggests an avenue for design optimization. The mechanism of stress inversion is explained as follows for flat and micro-engineered samples. In the first case, it is the cooling rate that controls the remaining residual stress after the end of a plasma cycle. If there is not enough cooling, plastic strain results from compression, and when the plasma stops impinging on the surface, the stress state is tensile. If enough cooling is supplied, the magnitude of reversed tensile stress is small. This is shown in Fig. 8. In the second case of the micropillar, the tension caused by the elastic expansion of the rhenium core causes tensile residual plastic strain, which upon cooling becomes compressive, as shown in Fig. 11.

Because the plastic strain in the model is derived from the Orowan relation ($\dot{\varepsilon} = bv_g\rho_m$) the glide velocity ($v_g$) is a key variable controlling the deformation of a body. Corresponding glide velocities for a planar high heat flux sample (HHFS), tapered micro-pillar (TMP), and non-tapered micro-pillar (NTMP) are compared in Fig. 11 for a given thermal loading scenario. The v_g for the tapered pillar is again shown to be markedly reduced compared to a flat W surface, and is a principal reason behind the resultant reduction of plastic strain in tapered pillars. This simple geometric change, allows more of the volume to distribute the body force generated due to plastic strain within the dendrite during a thermal transient event, and alleviates excessive plastic distortion. This reduces the chance of thermal cracking under repeated plasma loading.

3.4. Design of resilient surfaces

The stark difference in thermomechanical behavior between architectures suggested by Fig. 11 for the tapered and non-tapered variants of the pillars implies that surface features can be designed to accommodate a given thermal loading scenario. In light of this, surface geometry which promotes heat dissipation will be a favorable candidate for surface architectures in thermally aggressive environments. Fig. 12 demonstrates how changes in geometry such as taper vs. no-taper can impact the load seen by the pillar. For comparison, the Figure shows the temperature rise experienced by a thin (1.5 mm) plate with a conventional surface undergoing a 27 MW/m^2 heat pulse on one face, and actively cooled on the opposing face (h = 10 kW/m^2). Mitigation of the temperature rise in tapered pillars even for a significant heat flux of 27 MW/m^2 demonstrates the potential that surface micro-engineering may have in the development of new thermal shielding.

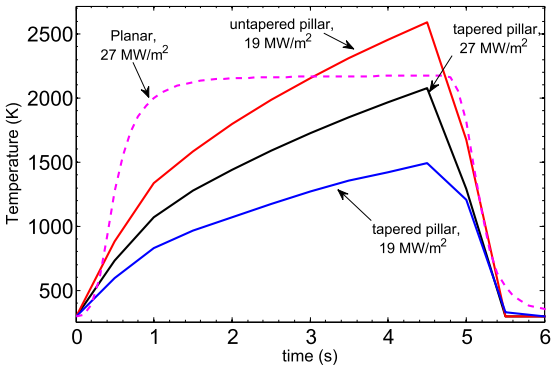

Fig. 12. Comparison of the temperature profile at the surface of an actively cooled (h = 10 kW/m^2) planar high heat flux sample (HHFS) and micro-pillars for a single 5 s pulse, note how the tapered micro-pillar maintains a lower temperature for a pulse of the same magnitude (27 MW/m^2).

A snapshot of the stress profiles across the W coating of a pillar undergoing a 27 MW/m^2 heat pulse is shown in Fig. 13. The stress is clearly concentrated at the Re-W interface, and decays towards the surface. Fig. 13 displays the residual stress along the thickness of the W coating after 6 pulses of 27 MW/m^2 intensity. The surface of the pillar can be seen to remain in a state of compressive stress, and can differ significantly in magnitude depending on the shape. It should be noted that the tapered pillar experiences a reduced residual stress even across the thinnest span of the coating (0.5 μm) relative to the un-tapered variant with W-coating that is twice as thick (1 μm). Factors such as the diameter of the Re core and W coating thickness will determine whether the surface stress present after the loading cycle will be tensile or compressive. These observations can be used to explain differences in the residual stress state measured by XRD and presented in Ref. [33]. From Fig. 13 it can be observed that thinner coatings will tend to remain in a state of residual compressive stress while thicker variants will tend

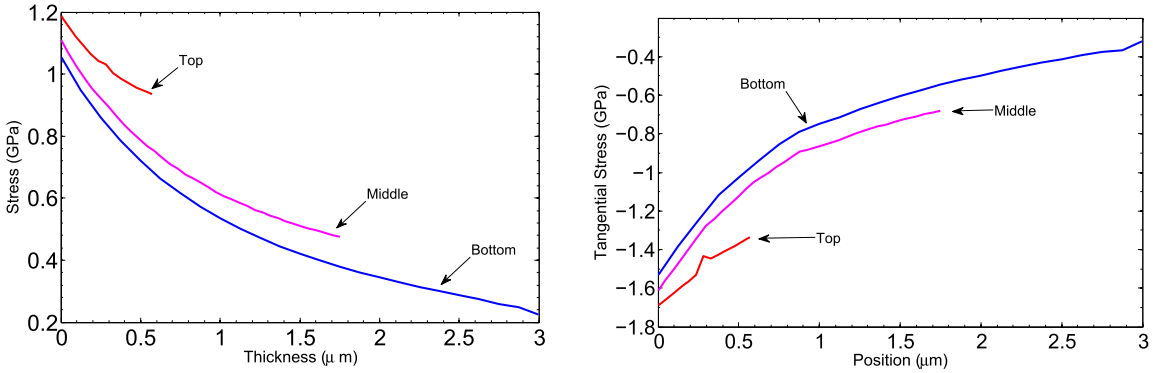

Fig. 13. Residual tangential stress profiles across the thickness of a tapered pillar at 3 s of a 5 s pulse, 27 MW/m^2 intensity, at different locations along the height, from the topmost region (T) where the thickness is the smallest ($\sim$ 0.5 μm) to the base of the pillar where the thickness is greatest (B) ($\sim$ 3 μm) residual stress in the W-coating. Broken lines represent straight W-Re dendrite, no taper, Re pillar (rod) radius = 2 μm, W-coating thickness is 1 μm, vs tapered pillar (solid lines), the tapered pillar profiles are taken at the end of 6 pulses or 43 s time, the 6 s snapshot for the non-tapered dendrite is the residual stress remaining after the initial pulse and illustrates ratcheting during the thermal cycle.

towards a tensile surface stress. This result denotes a range of pre-stress conditions an architected surface may be placed under for operation in a given environment. The pre-stress can be designated during the design phase of the material and modified to best conform to the needs of the application by a simple modification of geometric parameters such as coating thickness and core pillar diameter.

Due to the expansion constraints arising between W and Re, the maximum stress condition within the micro-pillar always arises at the interface between the two materials, in light of this, damage is terms of plastic flow or cracking is most likely to originate at this location. Because this interfacial stress is the maximum stress seen by the pillar, minimization of this quantity will lead to residual stress reduction. In fact, the interface condition between the Re core and the W coating is not as sharp as assumed in the present calculations. During plasma transients, inter-diffusion will take place between Re and W, thus giving gradual changes in their elastic properties across the interface. Based on available inter-diffusion data, we estimate that the Re-W interface will extend well into the W coating after only a few plasma transients. Thus, the interface stresses determined here are to be taken as upper bounds.

4. Conclusions

In this work, we presented a significant extension of the GMA viscoplasticity model, for simulations of plastic stress/strain distributions in materials undergoing cyclic thermal loading. The resulting plastic damage from the model is associated with fatigue-creep damage accumulation in materials exposed to cyclic high heat flux. The main motivation is to replace design rules of damage accumulation in mechanical components, where creep and fatigue phenomena are coupled and are hard to separate. Moreover, the model gives a desired link to the material's microstructure, where grain size, dislocation density and subgrains are described. Dislocation densities and subgrain evolution during thermomechanical cycles are well-described. Hence, the time dependence of microstructural features of plasma-facing components can be described in a way that is useful in assessing component reliability. Extension of the GMA model to polycrystalline materials within the framework of large deformation crystal plasticity has been demonstrated. The example studied here clearly shows large residual stresses at grain boundaries, which may result in grain boundary fracture or even grain ejection into the plasma.

Through direct comparison of the GMA viscoelasticity model and experimental results described in our work [33], we demonstrated the existence of a critical cooling rate, above which residual thermal stresses do not reverse and become tensile during the cooling part of the plasma cycle. It is shown experimentally and through modeling that if the effective heat transfer coefficient is less than 6 kW m^{-2} K^{-1}, large residual stresses build up on the surface, potentially leading to surface fracture. On the other hand, more aggressive cooling of plasma-facing surfaces results in the elimination of most of the tensile residual stress during the off-time of the plasma cycle.

A specific micro-engineered surface architecture that is composed on micro-pillars, each possessing an elastic Re core, and surrounded by a W shell has been designed, using CVD techniques. Unlike flat W surfaces that undergo tremendous compression during high heat flux plasma cycles, followed by stress several and potential surface fracture during the cooling cycle, the developed micro-engineered surfaces are shown to be quite resilient. Careful control of the W shell thickness and the Re core size of each micro-pillar through the CVD manufacturing process is shown to result in exactly the opposite behavior, as compared to flat W surfaces. The Re core first pushes on the W coating, putting it in tension during the heating phase, and when followed by contraction during the cooling phase of the plasma, the W-coating is put under compression. This would prevent surface fracture; which is a feature commonly observed in plasma-facing flat W samples. Subsequent plasma cycles are shown to result in the W coating mostly under compression, which is primarily caused by the pre-stress induced during the first few cycles.

The potential for development of materials with tailorable properties exists for plasma-facing components that are operating at extreme heat flux. For example, recent efforts on the development of fiber-reinforced composite tungsten have shown potential improvements in the thermomechanical properties [64–66]. Through modifications in surface geometry, it has been shown here that materials can be made to perform beyond their apparent intrinsic limits. The model presented here reveals that small changes in the geometry of micro-features making up the surface of W armor can markedly alter their residual stress state. This opens a pathway for optimization of armor concepts based on the design of constituent micron-scale entities comprising the surface. In the thermal loading scenario studied here, the temperature rise was the sole contributor to the generation of stress. Consequently, ideal geometric configurations that exhibit large surface areas for quick heat dissipation are expected to offer greater performance margins.

Acknowledgements

This work is partially supported by the Air Force Office of Scientific Research (AFOSR), Award No: FA9550-16-1-0444 with UCLA, and by the U.S. Department of Energy, Award Number DE-FG02-03ER54708 with UCLA. The technical assistance of Edward Gao with programming aspects of the GMA model is acknowledged.

References

[1] E.W. Parkes, Structural effects of repeated thermal loading, in: Benham, et al. (Eds.), Thermal Stress, Pitman, London, 1964.
[2] W. Jiang, F.A. Leckie, A direct method for the shakedown analysis of structures under sustained and cyclic loads, J. Appl. Mech. 59 (2) (1992) 251–260.
[3] J. Bree, Elastic-plastic behaviour of thin tubes subjected to internal pressure and intermittent high-heat fluxes with application to fast-nuclear-reactor fuel elements, J. Strain Analysis Eng. Des. 2 (3) (1967) 226–238.
[4] T.M. Mulcahy, Thermal ratcheting of a beam element having an idealized bauschinger effect, J. Eng. Mater. Technol. 98 (3) (1976) 264–271.
[5] Hany F. Abdalla, Mohammad M. Megahed, Maher YA. Younan, A simplified technique for shakedown limit load determination, Nucl. Eng. Des. 237 (12) (2007) 1231–1240.
[6] J. Zarka, F.C. Arnaudeau, J. Casier, G. Baylac, A practical method to determine elastic or plastic shakedown of structures, Simpl. methods Press. vessel analysis (1978).
[7] George Webster, Robert A. Ainsworth, High Temperature Component Life Assessment, Springer Science & Business Media, 2013.
[8] ASME, Boiler and Pressure Vessel Code, section iii, 1998.
[9] A.R.S. Ponter, S. Karadeniz, An extended shakedown theory for structures that suffer cyclic thermal loading, part 1: Theory, J. Appl. Mech. 52 (4) (1985) 877–882.
[10] H. Mecking, K. Lücke, Quantitative analyse der bereich iii-verfestigung von silber-einkristallen, Acta Metall. 17 (3) (1969) 279–289.
[11] Thomas H. Alden, Theory of plastic flow in strain-hardened metals, Philos. Mag. 25 (4) (1972) 785–811.
[12] H. Mecking, U.F. Kocks, Kinetics of flow and strain-hardening, Acta Metall. 29 (11) (1981) 1865–1875.
[13] Yu Estrin, L.S. Toth, A. Molinari, Y. Bréchet, A dislocation-based model for all hardening stages in large strain deformation, Acta mater. 46 (15) (1998) 5509–5522.
[14] F.B. Prinz, A.S. Argon, The evolution of plastic resistance in large strain plastic flow of single phase subgrain forming metals, Acta Metall. 32 (7) (1984) 1021–1028.
[15] L.P. Kubin, Yu Estrin, Evolution of dislocation densities and the critical conditions for the portevin-le chatelier effect, Acta metallurgica materialia 38 (5) (1990) 697–708.
[16] Garani Ananthakrishna, Current theoretical approaches to collective behavior of dislocations, Phys. Rep. 440 (4) (2007) 113–259.
[17] L.P. Kubin, C. Fressengeas, G. Ananthakrishna, Collective behaviour of dislocations in plasticity, Dislocations solids 11 (2002) 101–192.
[18] Daniel Walgraef, Elias C. Aifantis, On the formation and stability of dislocation patterns?i: one-dimensional considerations, Int. J. Eng. Sci. 23 (12) (1985) 1351–1358.
[19] Daniel Walgraef, Elias C. Aifantis, On the formation and stability of dislocation patterns?ii: two-dimensional considerations, Int. J. Eng. Sci. 23 (12) (1985) 1359–1364.
[20] Daniel Walgraef, Elias C. Aifantis, Dislocation patterning in fatigued metals as a result of dynamical instabilities, J. Appl. Phys. 58 (2) (1985) 688–691.
[21] Elias C. Aifantis, The physics of plastic deformation, Int. J. Plasticity 3 (3) (1987) 211–247.
[22] T. Kameda, M.A. Zikry, Three dimensional dislocation-based crystalline constitutive formulation for ordered intermetallics, Scr. Mater. 38 (4) (1998) 631–636.
[23] W.M. Ashmawi, M.A. Zikry, Effects of grain boundaries and dislocation density evolution on large strain deformation modes in fcc crystalline materials, J. computer-aided Mater. Des. 7 (1) (2000) 55–62.
[24] P. Shanthraj, M.A. Zikry, Dislocation density evolution and interactions in crystalline materials, Acta Mater. 59 (20) (2011) 7695–7702.
[25] P. Shanthraj, M.A. Zikry, Dislocation-density mechanisms for void interactions in crystalline materials, Int. J. Plasticity 34 (2012) 154–163.
[26] A. Arsenlis, D.M. Parks, Crystallographic aspects of geometrically-necessary and statistically-stored dislocation density, Acta mater. 47 (5) (1999) 1597–1611.
[27] Athanasios Arsenlis, David M. Parks, Modeling the evolution of crystallographic dislocation density in crystal plasticity, J. Mech. Phys. Solids 50 (9) (2002) 1979–2009.
[28] U.F. Kocks, H. Mecking, Physics and phenomenology of strain hardening: the fcc case, Prog. Mater. Sci. 48 (3) (2003) 171–273.
[29] Franz Roters, Philip Eisenlohr, Luc Hantcherli, Denny Dharmawan Tjahjanto, Thomas R. Bieler, Dierk Raabe, Overview of constitutive laws, kinematics, homogenization and multiscale methods in crystal plasticity finite-element modeling: theory, experiments, applications, Acta Mater. 58 (4) (2010) 1152–1211.
[30] M.E. Kassner, M.T. Perez-Prado, M. Long, K.S. Vecchio, Dislocation microstructure and internal-stress measurements by convergent-beam electron diffraction on creep-deformed cu and al, Metallurgical Mater. Trans. A 33 (2) (2002) 311–317.
[31] M.E. Kassner, P. Geantil, L.E. Levine, Long range internal stresses in single-phase crystalline materials, Int. J. Plasticity 45 (2013) 44–60.
[32] Nasr M. Ghoniem, J.R. Matthews, Robert John Amodeo, A Dislocation Model for Creep in Engineering Materials. Institute of Plasma and Fusion Research, University of California, Los Angeles, 1989.
[33] David Rivera, Richard Wirz, Nasr Ghoniem, Experimental measurements of surface damage and residual stresses in micro-engineered plasma facing materials, J. Nucl. Mater. 486 (2017) 111–121.
[34] Nasr M. Ghoniem, J.R. Matthews, Robert John Amodeo, A dislocation model for creep in engineering materials, Res. Mech. 29 (1990) 197–219.
[35] F.R.N. Nabarro, Theory of Crystal Dislocations, Oxford at the Clarendon Press, Oxford, England, 1967.
[36] J. Gittus, The mechanical equation of states: dislocation creep due to stresses varying in magnitude and direction, Philos. Mag. (1971) 1423–1440.
[37] R. Bullough, J.R. Willis, Stress-induced point defect-dislocation interaction and its relevance to irradiation creep, Philos. Mag. 31 (1975) 855.
[38] R. Bullough, M.W. Finnis, M.H. Wood, A theory of irradiation and thermal creep by dislocation climb, J. Nucl. Mater. 104 (1981) 1263.
[39] P.T. Heald, M.V. Speight, Steady-state irradiation creep, Philos. Mag. 29 (1974) 1075.
[40] M.E. Kassner, Recent developments in understanding the mechanism of five-power-law creep, Mater. Sci. Eng. A 410 (2005) 20–23.
[41] Robert J. Amodeo, Nasr M. Ghoniem, A review of experimental observations and theoretical models of dislocation cells and subgrains, Res. Mech. 23 (2–3) (1988) 137–160.
[42] D. Holt, Dislocation cell formation in metals, J. Appl. Phys. 41 (1970) 3197.
[43] A.S. Argon, S. Takeuchi, Steady-state creep of single-phase crystalline matter at high temperature, J. Appl. Mater. Sci. 11 (1976) 1542–1566.
[44] T.G. Langdon, Dislocations and creep, in: Proc. Conf. On Dislocations and the Properties of Real Materials vol. 221, Royal Society of London, 1984.
[45] K.D. Challenger, J. Moteff, Quantitative characterization of substructure of aisi-316 stainless-steel resulting from creep, Metall. Trans. 4 (1973) 749.
[46] D.J. Michel, J. Moteff, A.J. Lovell, Substructure of type 316 stainless-steel deformed in slow tension atdegrees C, Acta Metall. 21 (1973) 1269.
[47] I.J. Cuddy, Internal stresses and structures developed during creep, Metall. Trans. 1 (1970) 395.
[48] J.H. Gittus, Multiaxial mechanical equation of states for a work-hardening/recovery model of dislocation creep, Philos. Mag. 25 (1972) 1233.
[49] J.C.M. Li, Possibility of subgrain rotation during recrystallization, J. Appl. Phys. 33 (10) (1962).
[50] Rolf Sandstrom, Subgrain growth occurring by boundary migration, Acta Metall. 25 (1977) 905–911.
[51] Rolf Sandstrom, On recovery of dislocations in subgrains and subgrain coalescence, Acta Metall. 25 (1977) 897–904.
[52] Po Giacomo, Yinan Cui, David Cereceda, David Rivera, Tom D. Swinburne, Jaime Marian, Nasr Ghoniem, A phenomenological dislocation mobility law for bcc metals, Acta Mater. 119 (2016) 123–135.
[53] H.E. Evans, G. Knowles, Model of creep in pure materials, Acta Metall. 25 (1977) 963.
[54] E. Voce, The relationship between stress and strain for homogeneous deformation, Inst. Met. 74 (1948) 537.
[55] W.G. Johnson, J.J. Gilman, Dislocation velocities, dislocation densities, and plastic flow in lithium fluoride crystals, J. Appl. Phys. 30 (1950) 129.
[56] G.A. Webster, In support of a model of creep based on dislocation dynamics, Philos. Mag. 14 (1966) 775.
[57] U. Essmann, H. Mughrabi, Annihilation of dislocations during tensile and cyclic deformation and limits of dislocation densities, Philos. Mag. 40 (6) (1979).
[58] J.H. Gittus, Theoretical value of ratio (K) of cell diameter to dislocation spacing for a material undergoing dislocation-creep, Philos. Mag. 35 (1977) 293.
[59] J.H. Gittus, Theoretical relationship between free-energy and dislocation cell diameter during creep, Philos. Mag. A 39 (1979) 829.
[60] J. Friedel, Dislocations, Addison-Wesley Publishing Company, Inc., 1964.
[61] S.L. Robinson, O.D. Sherby, Mechanical behavior of polycrystalline tungsten at elevated temperature, Acta Metall. 17 (2) (1969) 109–125.
[62] Peter L. Raffo, Yielding and fracture in tungsten and tungsten-rhenium alloys, J. Less Common Metals 17 (2) (1969) 133–149.
[63] B. Gludovatz, S. Wurster, A. Hoffmann, R. Pippan, Fracture toughness of polycrystalline tungsten alloys, Int. J. Refract. Metals Hard Mater. 28 (6) (2010) 674–678.
[64] Bruno Jasper, Jan W. Coenen, Johann Riesch, Till Höschen, Martin Bram, Christian Linsmeier, Powder metallurgical tungsten fiber-reinforced tungsten, Mater. Sci. forum (2015).
[65] J. Riesch, Y. Han, J. Almanstötter, J.W. Coenen, T. Höschen, B. Jasper, P. Zhao, Ch Linsmeier, R. Neu, Development of tungsten fibre-reinforced tungsten composites towards their use in demo?potassium doped tungsten wire, Phys. Scr. 2016 (T167) (2016) 014006.
[66] R. Neu, J. Riesch, J.W. Coenen, J. Brinkmann, A. Calvo, S. Elgeti, C. García-Rosales, H. Greuner, T. Hoeschen, G. Holzner, et al., Advanced tungsten materials for plasma-facing components of demo and fusion power plants, Fusion Eng. Des. (2016).